Cancer Nanotechnology

RESEARCH Open Access

Boosting nuclear-targeted photothermal-chemotherapy by NIR-responsive hybrid membrane camouflaged nanotherapeutics

Xinyue Xing[1], Yuying Zeng[2], Wanqing Zhong[1], Wendai Cheng[1], Chengxin Zhou[1], Xiaoxu Lu[1*] and Liyun Zhong[3*]

*Correspondence:
hsgdzlxx@scnu.edu.cn;
zhongly@gdut.edu.cn

[1] Guangdong Provincial Key Laboratory of Nanophotonic Functional Materials and Devices, South China Normal University, Guangzhou, China
[2] Graduate School of Biomedical Sciences, Baylor College of Medicine, Houston, TX, USA
[3] China Guangdong Provincial Key Laboratory of Photonics Information Technology, Guangdong University of Technology, Guangzhou, China

Abstract

Background: Engineering nanotherapeutics have been extensively studied for cancer therapy. However, the therapeutic efficacy is still severely restricted by biophysiological barriers and intracellular accumulation. Although the biomimetic nanoparticles have improved the former issue, there is almost no breakthrough in researches of intracellular transport. Herein, we proposed a NIR-responsive nuclear-targeted hybrid membrane biomimetic Prussian blue drug-loading nanotherapeutics (PB@DN@M).

Results: The hybrid membrane coating bestows nanotherapeutics tumor targeting and immune escape ability, thus promoting the tumor enrichment of PB nanotherapeutics. The nuclear targeting function triggered by NIR enhances the cellular internalization and nuclear entry efficiency, resulting in a superadditive effect for boosting photothermal-chemotherapy efficacy. Moreover, taking advantage of non-interference Raman properties of PB, we can track the location and distribution of nanotherapeutics, which is beneficial for guiding precise synchronization of photothermal-chemotherapy. The results revealed that this PB@DN@M presented a remarkable therapeutic efficacy and significantly inhibited the tumor growth up to 87.17%.

Conclusions: Therefore, this spatiotemporal controllable biomimetic nanotherapeutics will provide a new insight and strategy for specific targeted therapy of tumors.

Keywords: Biomimetic hybrid membrane, Prussian blue nanotherapeutics, Nuclear-targeted photothermal-chemotherapy, SERS analysis

Background

Benefiting from the highly tunable property and easily functionalized surface of nanoparticles, multiple therapy modalities based on nanotherapeutics, such as chemotherapy (O'Brien et al. 2004; Singh et al. 2016; Arabi et al. 2015), radiotherapy (Boateng and Ngwa 2020; Pallares and Abergel 2020; Her et al. 2017) and phototherapy (Terentyuk et al. 2014; Espinosa et al. 2016; Liu et al. 2022) have been extensively applied in cancer

treatment. However, difficulties of overcoming physiological barriers involving the blood circulation and tumor penetration are seriously limited its therapeutic efficacy (Bourquin et al. 2018; Nel et al. 2009). Modification of poly(ethylene glycol) (PEG), the most common strategy to extend residence time of nanoparticles, is far from enough to cope with complex biological environments (Knop et al. 2010). Inspiring by red blood cells, Zhang et al. pioneered the cell membrane coating technology to prolong the circulation period of nanotherapeutics in vivo up to 72 h (Hu et al. 2011). The camouflage of synthetic nanomaterials with natural cell membranes allows the biomimetic nanoparticles to exhibit both the bio-interfacial functions and physicochemical properties. Since then, cell membrane biomimetic approach has emerged as a promising strategy for cancer theranostics (Bose et al. 2018; Rodriguez et al. 2013; Liu et al. 2020; Wang et al. 2020). In addition to single cell membrane, various hybrid membrane or engineered membrane has also been explored to satisfy diversified research needs (Liu et al. 2021a; Li et al. 2021).

Although the premature clearance of nanoparticles was improved by biomimetic nanotechnology, insufficient cellular uptake and intracellular trafficking are still resulting in the low drug delivery efficiency and poor therapeutic effect (Yang et al. 2019). The bioconjugation of high-affinity biomolecules including peptides, aptamers and antibodies to mediate organelle targeting of nanoplatforms has become the research hotpot of tumor-specific therapy and biomolecules detection (Singh et al. 2021; Maity and Stepensky 2016; Pan et al. 2012). For nucleus targeting, nuclear localization sequence peptides (NLS) with a characteristic sequence of Pro-Lys-Lys-Lys-Arg-Lys-Val (PKKKRKV) can transport nanoparticles into the nucleus by an active way (Kalderon et al. 1984). Therefore, by taking advantage of NLS, nanotherapeutics showed higher nuclear entry efficiency and more enriched target accumulation, which led to enhanced therapeutic efficacy (Shen et al. 2018; Tammam et al. 2016). Based on the organelle targeting strategy, it is promising to develop specific nanotherapeutics for precision medicine and accurate intracellular products analysis.

In order to administer photothermal-chemotherapy precisely, intracellular localization and distribution of nanotherapeutics is critical. Surface-enhanced Raman spectroscopy (SERS), renowned for its powerful fingerprint specificity and high sensitivity, provides unprecedented possibilities in biomedical sample analysis for the nanodrugs tracking as well as biochemical molecular imaging (Maiti et al. 2012; Tang et al. 2021; Cheng et al. 2020; Kapara et al. 2020). Prussian blue (PB) nanoparticles, possessing a sharp and strong Raman characteristic peak in the biological silence regent (1800–2800 cm^{-1}), are ideal Raman reporter, which can be employed for background-free SERS mapping (Yin et al. 2017). Besides, Prussian blue (PB) has also been permitted in biomedicine research by the U.S. Food and Drug Administration (FDA). It has been tremendously used for chemotherapy, phototherapy, MRI imaging and multimodal therapy (Lin et al. 2019; Zhu et al. 2020; Liu et al. 2021b).

Hence, we proposed a hybrid membrane biomimetic Prussian blue nanocarrier with nuclear targeting function (PB@DN@M) for enhanced photothermal-chemotherapy of hepatocellular carcinoma. In this PB@DN@M nanotherapeutics, the external hybrid membrane coating, derived from liver cancer cell (HepG2, HM) and macrophage (Raw 264.7, RM), present both the homotypic targeting ability of tumor cells and the

immune escape capability of macrophages, which can prolong the circulation life in blood and enhance the targeting to tumors. The internal Prussian blue (PB) nanocarrier was loaded with the anticancer drug doxorubicin (DOX) and functionalized with nuclear localization signal peptides (NLS). The external cell membrane coating not only avoids the premature leakage of DOX, but also prevents the formation of 'protein corona' of the nuclear localization signal peptide in blood circulation. After the PB@DN@M nanotherapeutics internalized by cells, the photothermal effect of PB NPs was triggered by NIR laser. Then, external hybrid membrane coating was destroyed and internal Prussian blue nanotherapeutics was transported to nucleus with the assistance of NLS accompanying by drug release. Trigger of photothermal therapy can not only promote the cell uptake and the nuclear entry efficiency of nanodrugs, but also increase the sensitivity of cells to chemotherapeutic agents. For another, chemotherapy implemented by DOX makes cells more sensitive to photothermal therapy and prevents tumor recurrence after photothermal therapy (Jędrzak et al. 2020; Li et al. 2018a), which achieved the enhanced therapeutic efficacy against hepatocellular carcinoma. It is hoped that this nuclear-targeted photothermal-chemotherapy biomimetic nanotherapeutics has the potential to become a new strategy for accurate tumor therapy.

Experimental sections

Materials and reagents

All reagents were commercially available and used as received. $FeCl_3{\cdot}6H_2O$ and doxorubicin hydrochloride (DOX) were purchased from Shanghai Aladdin Biochemical Technology Co., Ltd (China). $K_4[Fe(CN)_6]$ was achieved from Shanghai Macklin Biochemical Co., Ltd (China). Citric acid was obtained from Tianjin Zhiyuan Chemical Reagent Co., Ltd (China). Nuclear localization signal peptides (NLS, CGGPKKKRKVGG) and FITC-labeled NLS (FITC-NLS, CGGPKKKRKVGG-FITC) were purchased from Shanghai Apeptide Co.,Ltd (China). The cell counting kit-8 (CCK-8) were obtained from Dalian Meilun Biotechnology Co., Ltd (China). Membrane protein extraction kit, Hoechst 33342, mitochondrial membrane potential detection kit (JC-1), reactive oxygen species assay kit (DCFH-DA) and Calcein-AM/PI double stain kit were purchased from the Shanghai Beyotime Institute of Biotechnology (China).

Synthesis of PB@DN@M nanotherapeutics

PB NPs were synthesized according to previous work (Shokouhimehr et al. 2010). Briefly, 0.5 mmol citric acid was first added to 20 mL 0.5 mmol aqueous $FeCl_3{\cdot}6H_2O$ solution under stirring at 60 °C. Then, 20 mL of 0.5 mmol aqueous $K_4[Fe(CN)_6]$ solution containing 0.5 mmol citric acid was added. After stirring for 1 min at 60 °C, the solution was cooled to room temperature with the stirring for another 5 min. An equal volume of acetone was then added. The dispersion was centrifuged at 10,000 rpm for 15 min, washed three times with a mixture of deionized water and acetone. Finally, the precipitate was dried for use.

To load DOX on the PB NPs, 5 mL 1 mg/mL DOX aqueous solution water was mixed with 5 mg PB NPs in 10 mL deionized water under stirring at room temperature for overnight. Then, the mixture was centrifuged at 10,000 rpm for 15 min to obtain the DOX-loaded PB NPs (PB@D NPs). After that, 10 mL 1 mg/mL PB@D NPs solution was

added with 15 μL 1 mg/mL NLS or FITC-NLS solution and stirred in a weak-acid condition (pH 5–6) at room temperature for overnight. The excess NLS was removed by centrifuged at 10,000 rpm for 15 min. Then, the precipitate was redispersed in water for collecting nuclear-targeted PB@D NPs (PB@DN NPs).

To prepare hybrid membrane coating PB nanotherapeutics, HepG2 cell membrane, H22 cell membrane and Raw 264.7 cell membrane were extracted according to the manufacturer's instructions of the membrane protein extraction kit. Briefly, cells in PBS (pH 7.4, 4 °C) were scraped off with cell scrapers and collected by centrifugation at 600 *g* for 5 min. The collected cells were suspended in membrane protein extraction reagent A containing PMSF (1 mM). After incubating in an ice bath for 10 min, cell suspension was freeze-thawed twice between −80 ℃ and room temperature. The supernatant was further centrifuged at 14,000 *g* for 30 min to collect membrane, which was stored at −20 °C for further use. In order to obtain hybrid membrane (HM-RM, M), HepG2 and Raw 264.7 cell membrane were mixed at the membrane protein radio of 1:1 (w/w) and sonicated at 37 °C for 10 min. Finally, PB@DN NPs were mixed with hybrid membrane and extruded through a 200 nm, 100 nm, 50 nm polycarbonate porous membrane by a mini-liposome extruder (Avestin LiposoFast LF1, Canada).

Characterization of PB@DN@M nanotherapeutics

The morphology and diameter of biomimetic PB nanotherapeutics was characterized by TEM (JEOL JEM-1400PLUS, Japan). 1% (w/v) phosphotungstic acid was used for negative staining. The UV–vis spectra were acquired by UV–vis spectrophotometer (Shimadzu UV-2700, Japan). Zeta potentials of PB-based NPs were detected by a Micromeritics Zetasizer (Nano Plus-3 USA). The SERS spectra was scanned by Raman spectroscopy (Invia, Renishaw, UK). Each point was exposed for 3 s and integrated for twice to obtain the Raman spectrum. The extracted cell membrane proteins were characterized by using western blotting. The primary antibody CD81 (ab109201) and CD36 (ab133625) were achieved from Abcam.

Cells and animal models

HepG2 cell was obtained from the Sun Yat-sen University (Guangzhou, China). Raw264.7 cell was purchased from iCell Bioscience Inc (Shanghai, China). VE cell (human vascular endothelial cells) was purchased from BeNa Culture Collection (Beijing, China). All cells were cultured in DMEM medium (Gibco, USA) containing 10% fetal bovine serum (FBS, Gibco, USA) and 1% penicillin/streptomycin (Gibco, USA) at 37 °C in a 5% CO_2 incubator.

Female BALB/c mice (6–8 weeks, 20–22 g) were purchased from Guangzhou Ruige Biological Technology Co., Ltd (Guangzhou, China). The mice were adapted to the environment for a week before the experiment. All animal experiments were carried out in accordance with the National Guidelines for Experimental Animal Welfare and Ethics (China) and approved by Institutional Animal Care and Use Committee of South China Normal University (No. SCNU-313388). For in vivo studies, H22 cells were injected subcutaneously in the right armpit of BALB/c mice to establish the hepatoma model.

In vitro drug loading and release

The loading capacity (L.C.) and the encapsulation efficiency (E.E.) was measured by using a UV–vis absorbance spectrometer (UV-2700 Shimadzu, Japan) and calculated according to the following equation:

$$\text{E.E.}(\%) = \frac{M_{\text{t}} - M_u}{M_t} \times 100\%,$$

$$\text{L.C.}(\%) = \frac{M_{\text{t}} - M_u}{M_n + M_{\text{m}}} \times 100\%$$

where M_{t} represents the total mass of DOX, M_{u} is the mass of unencapsulated DOX, M_{n} is mass of NPs and M_{m} is the mass of hybrid membrane in NPs.

The release of DOX was measured with a dialysis method under four conditions: (1) pH 7.4 (without irradiation); (2) pH 5.0 (without irradiation); (3) pH 7.4 and irradiation with 785-nm laser (1 W/cm^2) for 5 min; and (4) pH 5.0 and irradiation with 785-nm laser (1 W/cm^2) for 5 min. Briefly, 2 mg PB@D@M NPs with/without NIR irradiation were loaded in dialysis bag immersed in 20 mL released buffer PBS (pH 7.4 or 5.0) for overnight, respectively. At the predetermined time points, 2 mL of the external PBS was withdrawn and replaced with an equal volume of fresh PBS. The concentration of DOX in the released buffer was analyzed by a UV–vis absorbance spectrometer.

Evaluation of photothermal properties

The photothermal conversion ability of different concentrations of PB NPs and PB@M NPs were evaluated by irradiation with 785-nm laser (1 W/cm^2) for 5 min. Temperature changes were monitored by an infrared thermal imager (Fluke Ti400, USA).

Homotypic targeting ability of PB@D@M NPs

VE cells, HeLa cells and HepG2 cells were seeded into the gold film substrates/cover glass (1×10^5 cells/well) in 6-well plates for 12 h, respectively. Then the PB@D@M NPs (37 μg/mL) were added and incubated for another 6 h. After fixed by paraformaldehyde, the samples were used for SERS mapping. The scanning step was set as 0.5 μm and the integration time was 1 s for each point. For fluorescence imaging (Olympus IX73, Japan), the paraformaldehyde-fixed cells were dyed with Hoechst 33342 for imaging. In addition, atomic force microscopy (NTEGRA Probe NanoLaboratory, NT-MDT, Russia) imaging was also used to analyze the targeting ability.

Immune escape ability of PB@D@M NPs

Raw 264.7 cells were seeded into the cover glass in 6-well plates (1×10^5 cells/well) for overnight. Then the media were replaced by the media containing PB@D, PB@D @HM and PB@D@M NPs (37 μg/mL). The cells were incubated for 6 h and fixed by paraformaldehyde and stained with Hoechst 33342 for fluorescence imaging.

Nuclear targeting ability of PB@DN@M NPs

ICP analysis and fluorescent imaging were employed to verify the nuclear targeting of biomimetic PB NPs. Briefly, HepG2 cells were seeded into the Petri dish (1×10^5 cells/well) for overnight. Then the media were replaced with the media containing PB@HM, PB@RM NPs, PB@M and PB@N@M NPs (37 μg/mL) for 8 h. For photothermal triggering, cells incubation with PB@N@M NPs was irradiation with/without 785-nm laser (1 W/cm^2) for 5 min and culture for another 4 h. After that, the samples were collected for ICP (SPECTRO ARCOS MV, Germany) detection. For fluorescence imaging, the nuclear-targeted PB NPs were replaced with FITC-labeled nuclear targeting PB NPs.

Cytotoxicity of PB@DN@M NPs in vitro

HepG2 cells were seeded into a 96-well plate (1×10^4 cells/well) for 24 h. PBS, DOX and PB@N@M NPs at the same DOX concentrations were added to cells and incubation for 8 h. The cells were irradiated with or without 785nm laser (1 W/cm^2) for 5 min and further incubated for another 4 h. Then, CCK-8 assay was performed to evaluate the cell viability according to the manufacture's instruction. The absorbance at 450 nm was recorded using a microplate reader (Bio-Rad, USA).

Live/dead cell staining assay

To confirm the cytotoxicity of the designed nanotherapeutics, live/dead cell staining assay was used. HepG2 cells were seeded into a 6-well plate (1×10^5 cells/well) for 24 h. PB@DN@M NPs were added to cells and incubation for 8 h. Then, the NPs was irradiation with/without 785nm laser (1 W/cm^2) for 5 min and culture for another 4 h. The resulting cells were stained with calcein-AM/PI and observed with fluorescence microscopy (Olympus IX73, Japan).

Intracellular ROS levels

The intracellular ROS levels were detected by reactive oxygen species assay kit (DCFH-DA) according to the manufacture's instruction. The cells incubated PB@DN@M were observed by using fluorescence microscopy.

Mitochondrial membrane potential detection

The membrane potential detection kit (JC-1) was used to determine the charge of mitochondrial membranes. After staining with JC-1, fluorescent intensity of HepG2 cells incubated with PB@DN@M NPs was recorded by a fluorescence spectrophotometer (F-4600, Hitachi, Japan).

In vivo tumor growth inhibition investigations

The H22 tumor-bearing BALB/c mice were divided into six groups according to the different treatments ($n = 5$ per group): (1) PBS, (2) PB NPs (with PB concentration at 5 mg/kg), (3) PB@DN@M NPs (5 mg/kg), (4) NIR irradiation, (5) PB NPs with NIR irradiation (with PB concentration at 5 mg/kg), (6) PB@DN@M NPs (5 mg/kg) with NIR irradiation. All the samples were intravenously injected into mice via the tail

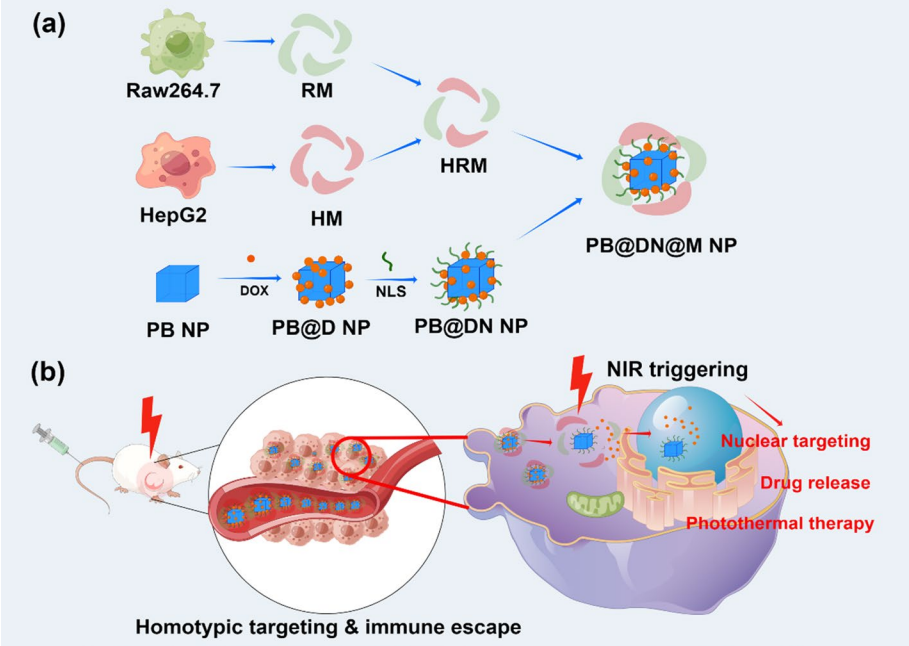

Scheme 1 **a** Fabrication of the nuclear-targeted hybrid membrane biomimetic Prussian blue DOX-loading nanocarriers (PB@DN@M). **b** Synergistic photothermal-chemotherapy of PB@DN@M against hepatocellular carcinoma (by FigDraw)

vein. For photothermal therapy, the mice were irradiated with 785nm laser (1 W/cm^2) for 5 min after the PB nanotherapeutics were injected for 12 h. The tumor volume and mouse body weight were measured every day. After 20 days, all the mice were euthanized and the major organs and tumors were collected for H&E staining and SERS mapping. The TGI rate was calculated according to the following equation:

$$\mathrm{TGI} = \frac{V_c - V_t}{V_c} \times 100\%,$$

where V_c is the tumor volume of the control group and V_t is the tumor volume of the other groups.

After injection with PB nanotherapeutics for overnight, the major organs and tumor tissues were gathered and dissolved in hypochlorite–nitric acid (1:3 v/v). The Fe contents in organs and tumors were measured with ICP to determine the biodistribution of PB nanotherapeutics.

Statistical analysis

Experimental data were given as the mean ± standard deviation (SD) ($n \geq 3$). One-way analysis of variance method was adopted to evaluate the significance level of the experimental data between groups through Graph Pad Prism version 9.0 software. A p value of 0.05 was selected as the significance level, and all data were marked as * for $p < 0.05$, ** for $p < 0.01$, *** for $p < 0.001$ and **** for $p < 0.0001$.

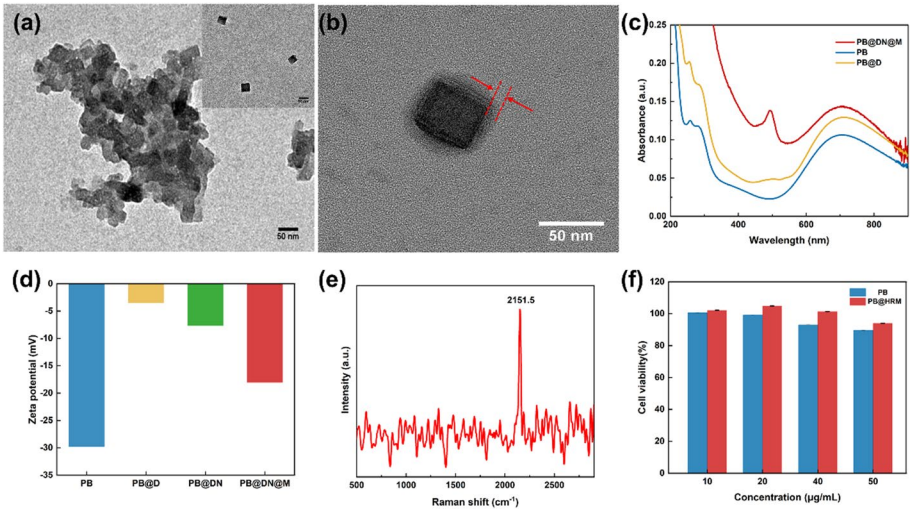

Fig. 1 Characterization of biomimetic PB nanotherapeutics. TEM images of **a** PB NPs and **b** PB@M NPs. Scale bar: 50 nm. **c** UV–Vis absorption spectra of PB-based NPs. **d** Zeta potential of PB-based NPs. **e** SERS spectra of PB@DN@M NPs. **f** Cell viability of HepG2 cells incubated with different concentrations of PB-based NPs for 24 h

Results and discussion

Characterization of PB@DN@M nanotherapeutics

PB@DN@M NPs were synthesized following Scheme 1. The morphology and diameter of biomimetic PB nanotherapeutics were characterized by TEM (Fig. 1a, b). The fabricated PB NPs exhibited a monodisperse cubic structure with a diameter of ~ 36 nm. After cloaking with hybrid membrane, the surface of PB NPs was covered with an outer shell thickness of ~ 8 nm, which was consistent with previous reports (Wang et al. 2018). The UV–vis absorption spectrum in Fig. 1c revealed the spectral change during the construction of biomimetic PB nanotherapeutics. PB NPs appeared a wide and strong absorption band in NIR region between 600 and 900 nm, with a centered peak at 703 nm. Accordingly, PB@DN@M NPs displayed a similar absorption band except a slight red shift. Besides, a new absorption peak at 499 nm was observed in PB@D NPs and PB@DN@M NPs, indicating the loading of DOX. In comparison with PB@D NPs, PB@DN@M NPs presented much higher peak intensity of DOX, which was attributed to the reduction of drug leakage by hybrid membrane coating. To further investigate the synthesis of PB@DN@M NPs, surface zeta potential of PB NPs before and after modification was measured (Fig. 1d). Following hybrid membrane coating, the surface potential of PB changed from − 29.85 mV to − 18.06 mV, thus confirming the camouflage of negatively charged outer membrane layer. As evidenced by Raman spectrum in Fig. 1e, PB NPs showed a strong and sharp characteristic peak at 2152 cm^{-1} in the Raman silent region, assigning to the stretching vibration of C≡N (Zhu et al. 2020), which guaranteed the accuracy in SERS analysis due to avoid the spectral crosstalk and overlap. The biocompatibility of nanoparticles is an essential concern in nanotherapeutic research. The CCK-8 assay suggested that PB@M NPs presented higher cell viability than PB NPs owing to the presence of biocompatible cell membrane coating. For characterizing the membrane extraction,

western blotting was carried out to analyze the membrane protein (Additional file 1: Fig. S1). The hybrid Hep-Raw membrane was mixed at the membrane protein radio of 1:1 w/w with the optimal balance between prolonged blood circulation and homotypic targeting, which can exhibit higher tumor accumulation and better PTT efficacy (Jiang et al. 2019). The HepG2-specific membrane protein CD36 was revealed on the HepG2 membrane and hybrid Hep-Raw membrane. Meanwhile, the macrophage-specific membrane protein CD81 was detected on the Raw 264.7 membrane and hybrid Hep-Raw membrane. It demonstrated the successfully preparation of hybrid Hep-Raw membrane. Furthermore, the loading efficiency of PB were calculated according the calibration curve of DOX measured by UV–vis spectrophotometer. the loading capacity (L.C.%) and encapsulation efficiency (E.E.%) of PB@DN@M was 30.05% and 47.14%, which may attributed to the electrostatic interaction between PB NPs and DOX, as well as the coordinative bonding between inherent Fe(III) in the structure of PB NPs and chemical group (–OH, $–NH_2$) of DOX (Cai et al. 2015).

Photothermal properties of PB@D@M nanotherapeutics

PB NPs have drawn enormous concern for the reason of its high photothermal conversion efficiency. To assess the photothermal conversion property, the concentration-dependent temperature changes of PB NPs and PB@M NPs were recorded (Fig. 2a–d). Tumor cells/tissues can be immediately destroyed within a few minutes while the hyperthermia temperature increased above 50 °C. As shown in Fig. 2a, b, the temperature of 45 μg/mL PB NPs and 37 μg/mL PB@M NPs increased rapidly to 58 °C and 53.5 °C after the 785nm laser irradiation (1 W/cm^2) for 5 min, respectively. Thereby, the concentrations of 45 μg/mL for PB NPs and 37 μg/mL for PB@M NPs were selected for photothermal therapy. On the contrary, the temperature of water only increased by 10.2 °C under laser irradiation for 5 min. PB NPs presented high molar extinction coefficient and photothermal property under NIR laser, which could be ascribed to the energy change induced by the charge transition between Fe(II) and Fe(III) in PB NPs (Fu et al. 2012). It is clear that PB NPs before and after membrane coating displayed almost the same temperature distribution, implying the negligible impact of the membrane coating on the photothermal effect of PB NPs. In view of the long-term usage of PB nanotherapeutics in tumor therapy, the photostability of PB@M NPs were investigated. Figure 2c indicates that PB@M NPs still remained excellent photothermal stability after 5 cycles of laser irradiation.

The in vitro release of was also performed under different conditions. Apparently, PB@D@M NPs exhibited pH- and photo-responsive release characteristics. Without NIR laser irradiation, the cumulative release rate of DOX slightly increased from 26.11%.

At pH 7.4 to 41.22% at pH 5.0 within 24 h, which was mainly caused by the increased solubility of DOX in a weak acidic environment. Contrarily, with the trigger of NIR laser, the cumulative release at pH 7.4 and pH 5.0 was increased to 52.36% and 73.03%. The enhanced DOX release may be attributed to local hyperthermia produced by PB NPs which destroy the cell membrane coating and the pyrolytic separation of the electrostatic interactions between DOX and PB NPs, thus accelerating the diffusion of DOX into surrounding environment (Li et al. 2018b). Moreover, the intracellular drug release was explored by fluorescent imaging as illustrated in Fig. 2f. PB@D@M NPs with NIR

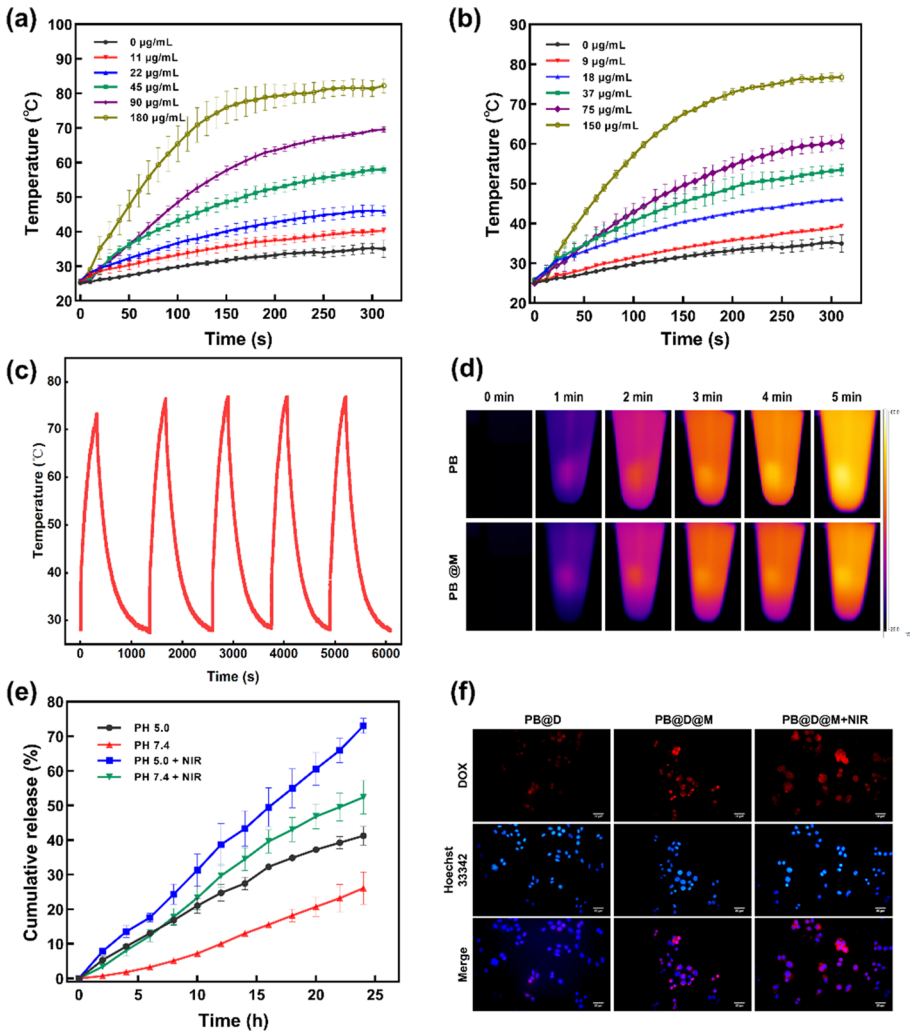

Fig. 2 Photothermal effect of biomimetic PB nanotherapeutics. **a** Temperature profiles of different concentrations of PB NPs under 785-nm laser irradiation (1 W/cm^2) for 5 min. **b** Temperature profiles of different concentrations of PB@M NPs under 785-nm laser irradiation (1 W/cm^2) for 5 min. **c** Photostability of PB@M NPs (150 μg/mL) under 785-nm laser irradiation (1 W/cm^2) for 5 cycles. **d** Representative photothermal images of 45 μg/mL PB NPs and 37 μg/mL PB@M NPs under 785-nm laser irradiation (1 W/cm^2) at various irradiation time points. **e** DOX release from PB@D@M NPs at pH 7.4 and 5.0 without or with 785-nm laser irradiation (1 W/cm^2) for 5 min. **f** Fluorescent images of intracellular DOX release from PB@D@M NPs without or with 785-nm laser irradiation (1 W/cm^2) for 5 min. Scale bar: 50 μm

irradiation exhibited the highest intracellular DOX fluorescence intensity in comparison with PB@D NPs and PB@D@M NPs, verifying the homotypic targeting ability of outer hybrid membrane coating and local hyperthermia enhanced-drug release.

Cellular uptake and distribution of PB@DN@M nanotherapeutics

As previously studied, exogenous NPs were easily recognized and cleared by host mononuclear phagocyte system (MPS), resulting in the insufficient accumulation in vivo (Dhas et al. 2022; Harris et al. 2019). In an attempt to improve the circulation and internalization, PB NPs were camouflaged with cancer–macrophage hybrid cell membranes. Macrophage membrane coating endows NPs with surprising immune evasion ability, while

the homologous adhesion proteins in cancer cell membrane gives NPs tumor homotypic targeting (Liu et al. 2019). The uptake of PB@M NPs by the VE, HeLa and HepG2 cells were visualized by SERS mapping based on the peak of 2152 cm^{-1}. Obviously, HepG2 cells displayed the strongest SERS peak intensity and distributions compared to VE and HeLa cells (Fig. 3a). Likewise, fluorescent images of VE, HeLa and HepG2 cells incubated with PB@M NPs in Additional file 1: Fig. S2 showed identical fluorescence intensity trends. The AFM images in Fig. 3c were also performed to verify the superiority of cancer–macrophage hybrid cell membranes in homotypic targeting. In contrast to PB NPs and single membrane camouflaged-PB NPs, HepG2 cells cultured with PB@HRM appeared the highest cell atomic force and adhesion, suggesting the best uptake efficiency. This demonstrated that the PB@M NPs possessed higher self-targeting capability derived from the HepG2 cell membrane and the longer circulation time inherited from the Raw 264.7 cell membrane. Fluorescent images of Raw 264.7 cells incubated with PB@D, PB@D@HM and PB@D@M NPs for 6 h were also obtained (Additional file 1: Fig. S3). Cell membrane especially hybrid membrane camouflaged-PB NPs showed little fluorescence intensity in comparison with uncloaked-PB NPs, thereby confirming the immune escape capability of biomimetic PB NPs. Furthermore, the nuclear targeting of PB@DN@M NPs was validated by ICP analysis and fluorescence imaging. The

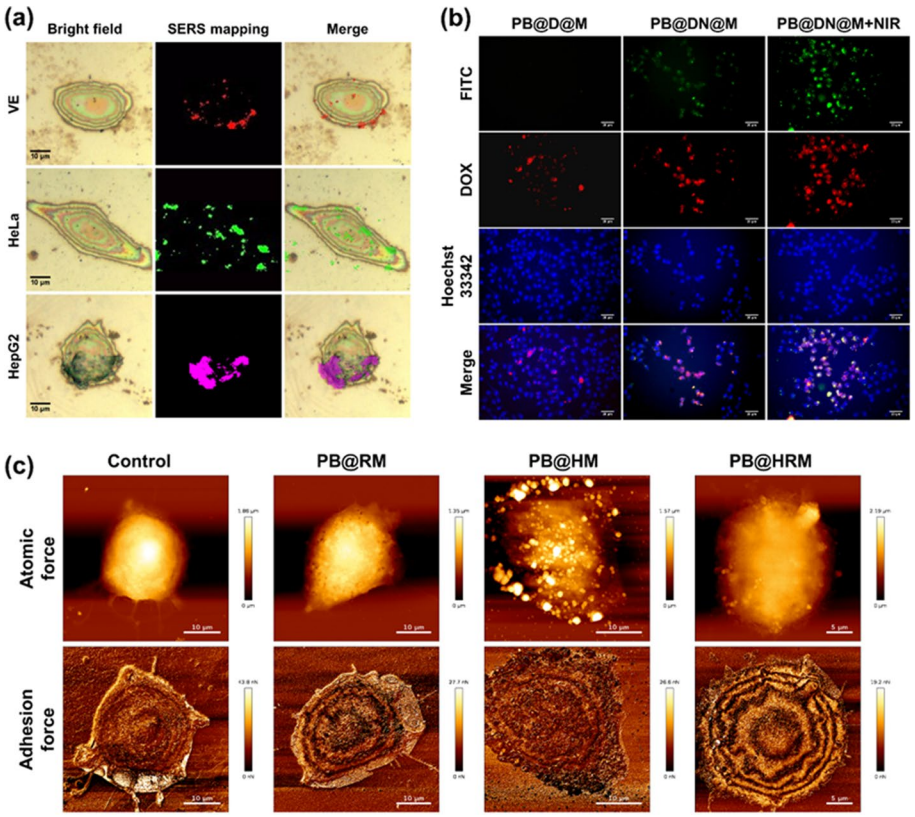

Fig. 3 **a** Bright-field and SERS images of VE cells, HeLa cells and HepG2 cells incubated with PB@M NPs for 6 h based on the peak of 2152 cm^{-1}. Scale bar: 10 μm. **b** Fluorescent images of HepG2 cells incubated with PB@D@M and FITC-PB@DN@M NPs without/with NIR irradiation. Scale bar: 50 μm. **c** AFM images and its adhesion mapping of HepG2 cells incubated with PB@HM, PB@RM and PB@M NPs for 6 h. Scale bar: 10 μm

PB contents (Additional file 1: Fig. S4) and fluorescence intensity (Fig. 3b) inside PB@DN@M NPs-treated HepG2 cells were higher than that of PB@M NPs-treated cells, indicating preferable internalization of PB@DN@M NPs by cells, which was caused by the slightly exposure of NLS in a weak-acid environment inside cancer cells. Especially, after irradiated by NIR for 5 min, the PB contents and fluorescence intensity inside nucleus increased dramatically, which may be due to the improvement of cell membrane permeability and switch-on of nucleus targeting triggered by PB NPs-induced photothermal effect. Therefore, the cancer–macrophage hybrid membrane enabled PB@DN@M NPs to possess tumor homotypic targeting and immune escape capability. Importantly, the incorporation of NLS significantly promoted the cell uptake and nuclear enrichment after NIR triggering.

In vitro antitumor performance of PB@DN@M nanotherapeutics

The in vitro antitumor activity of PB@DN@M nanotherapeutics was evaluated by CCK-8 assay and live/dead cell staining. As shown in Fig. 4a, the PB@DN@M NPs without/with the NIR irradiation presented 12.71% and 76.43% of cytotoxicity against HepG2 cells. By contrast, almost 40.44% cells were killed when cells were treated the PB@N@M NPs irradiated with NIR laser. For DOX treated cells, there was little difference in cytotoxicity

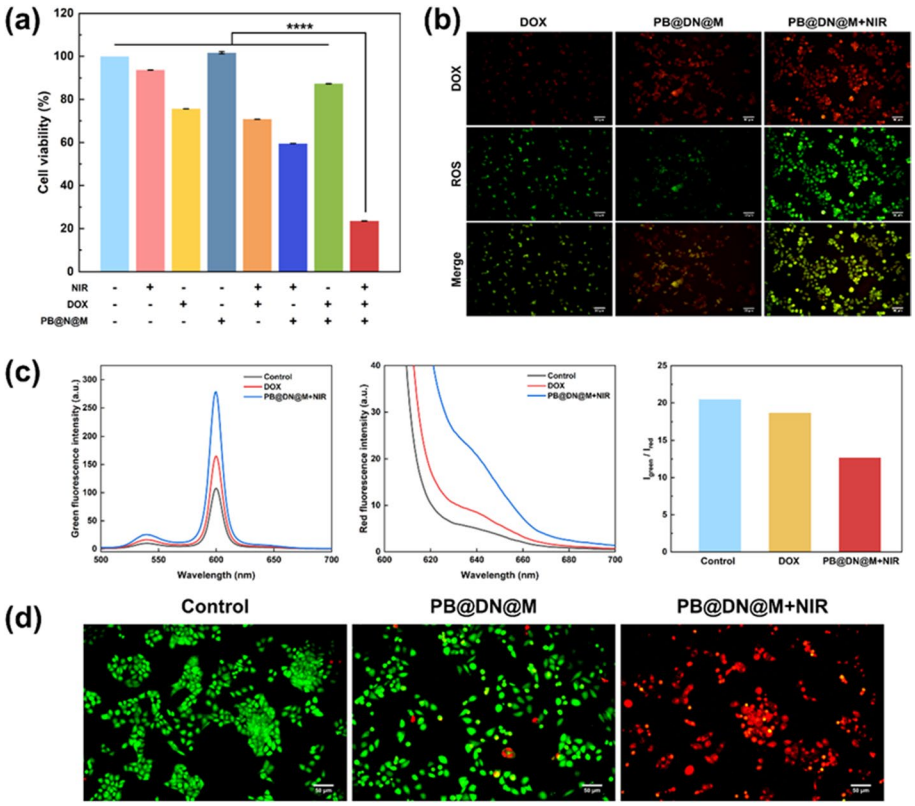

Fig. 4 In vitro antitumor activity of PB@DN@M NPs. **a** Cell viability of HepG2 cells after different treatment. ****$P < 0.0001$ **b** Fluorescent images of intracellular ROS accumulation during the DOX, PB@DN@M and PB@DN@M + NIR-induced cell death. Scale bar: 50 μm. **c** Mitochondrial membrane potential changes of HepG2 cells during DOX, PB@DN@M and PB@DN@M + NIR-induced cell death measured by JC-1 kit. **d** Fluorescent images of HepG2 cells stained with calcein-AM (green, live cells) and PI (red, dead cells) after PB@DN@M with/without NIR treatment. Scale bar: 50 μm

with (29.22%) or without (24.4%) NIR irradiation. The live/dead staining images (Fig. 4d) were similar to that of CCK-8 results. After irradiated by NIR laser for 5 min, almost all HepG2 cells incubated with PB@DN@M NPs were dead (stained by PI with red fluorescence). On the contrary, the control group and PB@DN@M treated-cells still survived in large amounts. Moreover, the intracellular ROS accumulation and mitochondrial membrane potential changes during the photothermal-chemotherapy were also measured by fluorescent analysis. Both results illustrated that HepG2 cells incubated with PB@DN@M NPs under the NIR irradiation had the highest ROS production and the fastest decrease in mitochondrial membrane potential. Taken together, the PB@DN@M NPs-induced photothermal-chemotherapy considerably inhibited hepatocellular carcinoma cells proliferation.

On the basis of no-interference Raman reporter PB, intracellular distribution of biomimetic nanotherapeutics and macromolecular information changes of HepG2 cells during photothermal-chemotherapy were achieved (Fig. 5a). Compared to PB@D NPs, HepG2 cells incubated with PB@DN@M NPs considerably internalized more NPs. Especially for the NIR triggered PB nanotherapeutics, PB@DN@M NPs distributed more concentratedly and evenly in the nucleus, which further demonstrated the tumor targeting and NIR-responsive nuclear targeting of hybrid membrane coating.

Molecular profiles of HepG2 cells during PB-induced photothermal-chemotherapy were also revealed by SERS spectroscopy. The significant changes of biomolecules after photothermal-chemotherapy were protein degradation, protein denaturation and DNA damage, summarized in Additional file 1: Table S1 (Ali et al. 2016; Xie et al. 2020; Zhao et al. 2020; Panikkanvalappil et al. 2016a, b; Nair et al. 2020; Huang et al. 2003; Qi et al. 2018). As shown in Fig. 5b, upon NIR irradiation, the Raman peak at 520 cm^{-1} exhibited a tremendous increase, which was attributed to S–S stretching in proteins surrounding on the PB nanotherapeutics. Similarly, a decline in the intensity of Raman band at 450 cm^{-1} and an increase in intensity at 583 cm^{-1} indicated the exposure of Trp residues due to the disruption of tertiary protein structure via S–S bond breakage,

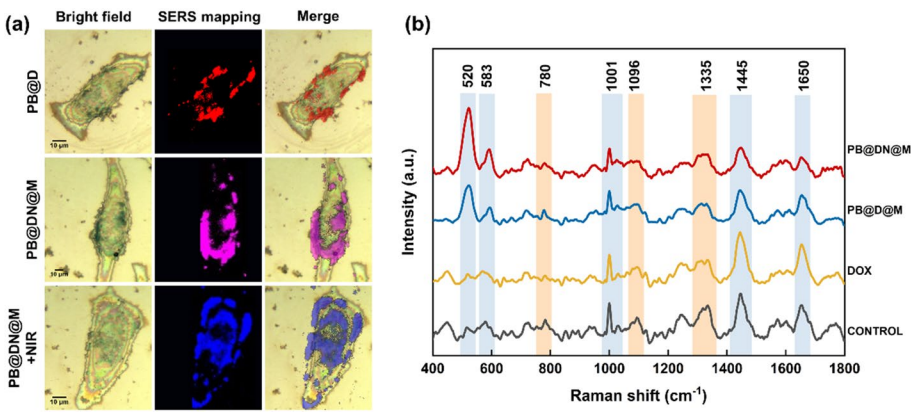

Fig. 5 SERS analysis of HepG2 cells incubated with PB@DN@M NPs under NIR irradiation for 5 min. **a** Bright-field and SERS images based on the peak of 2152 cm^{-1} of HepG2 cells incubated with PB@D, PB@DN@M NPs for 8 h and then cultured for another 4 h after NIR irradiation. Scale bar: 10 μm. **b** Normalized SERS spectra of HepG2 cells incubated with DOX, PB@D@M and PB@DN@M NPs for 8 h and then cultured for another 4 h after NIR irradiation

suggesting that the conformational change of cellular proteins led to cell death during PB therapeutics-induced photothermal-chemotherapy. The Raman characteristic band around 1001 cm^{-1} increased in intensity, owing to the benzene ring breathing of Phe during cell death. Importantly, it was demonstrated that the elevated levels of Phe was associated with mitochondria-mediated apoptosis via Rho/ROCK pathway and Fas/Fas ligand mediated apoptosis (Ali et al. 2016). In addition, the Raman peaks at 1245 cm^{-1} and 1650 cm^{-1}, assigned to β-sheet of amide III and α-helix of amide I respectively, was observed a decline in intensity due to the destroy of proteins conformation. The CH_2 bending along with methylene deformation in proteins and lipids appeared around 1445 cm^{-1}, which decreased gradually in the PB-induced cell death process. For DNA, a decrease in the peak at 780 cm^{-1} and 1096 cm^{-1}, assigning to O–P–O stretching from DNA backbone, represented the DNA damage during cell death. The Raman bands at 720 cm^{-1} and 1335 cm^{-1}, attributed to ring breathing of A, showed the same drop. Overall, we monitored the main events after the PB nanotherapeutics-induced cell death by SERS technique. Molecular changes involving protein denaturation, protein degradation and DNA damage were identified by the unique fingerprint spectra. The SERS analysis proved the boosted therapeutic efficacy of PB@DN@M-induced photothermal-chemotherapy as well as the potency of PB as a SERS tracker.

In vivo tumor growth inhibition investigations of PB@DN@M nanotherapeutics

Inspired by the excellent therapeutic effects in vitro, in vivo tumor growth inhibition experiments of PB@DN@M nanotherapeutics were explored in the murine hepatoma model illustrated in Fig. 6a. In order to estimate the in vivo photothermal effects, photothermal images was captured by an infrared thermal camera after the BALB/c mice intravenously injected in the tail vein with PBS, PB NPs and PB@DN@M NPs for 12 h, which may display the highest biomimetic PB NPs accumulation in tumor tissues. For the control mice, the temperature of tumor site only increased to 39.3 °C, while that of mice treated with PB NPs and PB@DN@M increased to 50.9 and 54.7 °C under the NIR laser irradiation for 5 min (Fig. 6c). It suggested that PB@DN@M NPs can efficiently absorb the NIR light energy and convert into local heat in vivo. To evaluate the in vivo performance of PB@DN@M NPs for nuclear-targeted photothermal-chemotherapy, the tumor-bearing mice were divided into six groups ($n = 5$) randomly with different treatment. After treatment for 20 days, all the mice were killed to collect tumors and major organs for next investigations. As evidenced by Fig. 6b–g, compared to other groups, PB@DN@M NPs with NIR irradiation treatment group presented awesome antitumor effect with the tumor growth inhibition (TGI) rate up to 87.17%. The digital photographs of tumors also indicated that the tumor size after nuclear-targeted photothermal-chemotherapy was much smaller than that of other groups. By contrast, the PB NPs under NIR irradiation and PB@DN@M NPs without NIR irradiation appeared TGI rate of 41% and 14.08%, respectively. There was no remarkable tumor inhibition effect in both NIR-irradiation and PB NPs-treated groups compared with control group. Correspondingly, the weight of tumors (Fig. 6g) at the end of the treatment were recorded, which was in agreement with tumor volume results in Fig. 6e. Meanwhile, Fig. 6f did not show any drastic decrease in mice body weight throughout the treatment, indicating the biosafety of PB@DN@M NPs.

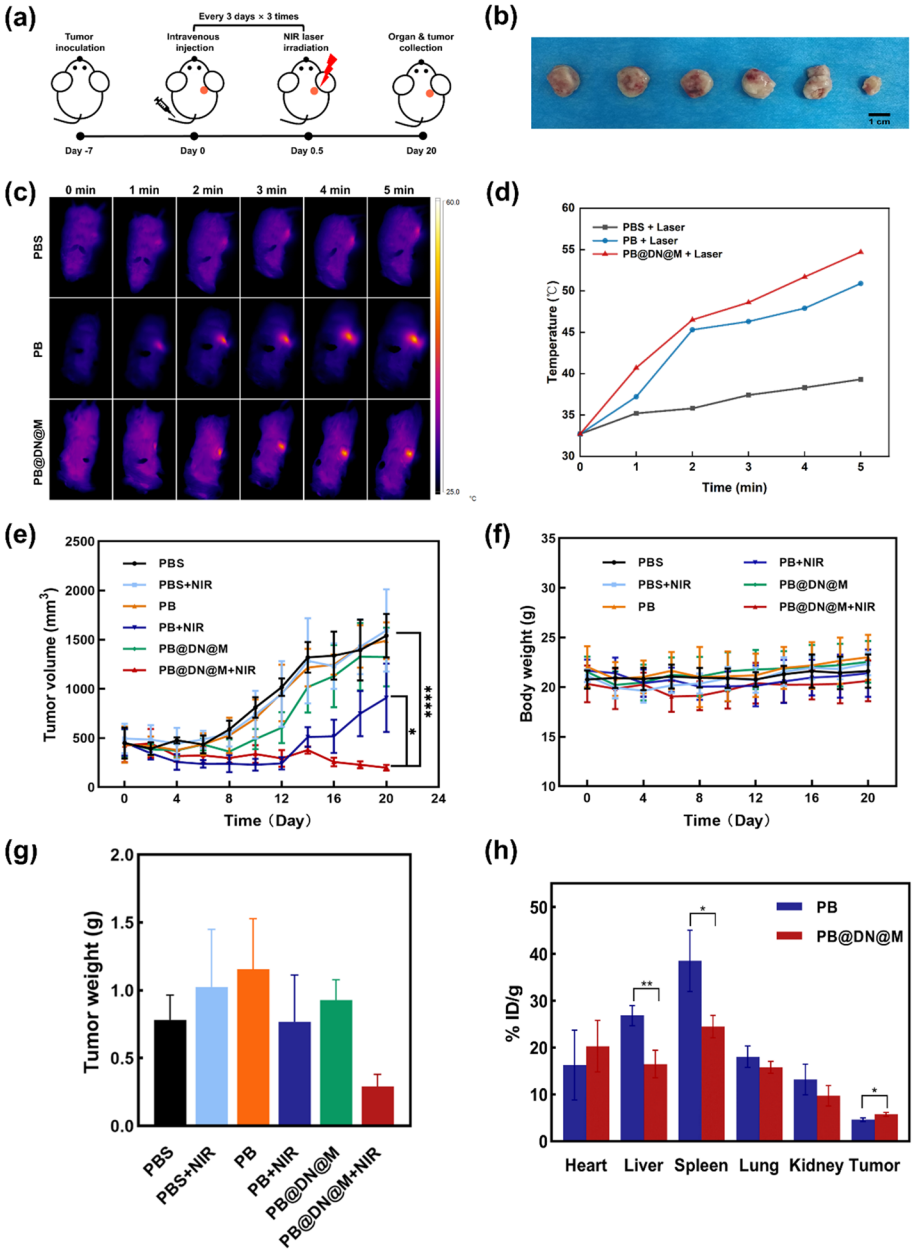

Fig. 6 **a** Schematic illustration of the in vivo therapeutic process. **b** Digital photographs of tumors collected from different groups after 20 days of treatment. Left to right: PBS, PBS with NIR irradiation, PB NPs, PB NPs with NIR irradiation, PB@DN@M NPs, PB@DN@M NPs with NIR irradiation. Scale bar: 1 cm. **c** Infrared thermal images and **d** corresponding temperature changes of liver tumor-bearing mice under NIR irradiation for 5 min. **e** Tumor volumes and **f** body weight of tumor-bearing mice after different treatments. **g** Tumor weights of different groups at the end of treatment. **h** Biodistribution of PB NPs and PB@DN@M NPs over a span of 12 h after injection

It was clear that the PB@DN@M NPs displayed superior photothermal conversion and highly tumor accumulation capacity, resulting in enhanced photothermal-chemotherapy potency involving hyperthermic tumor ablation and NIR-responsive drug release in vivo.

To certify the in vivo biodistribution of PB NPs and PB@DN@M NPs, tumors and major organs of the mice were collected to further study by ICP analysis. As shown in Fig. 6h, the PB@DN@M NPs displayed a significant higher tumor accumulation than that of PB NPs ($p < 0.05$), which indicated the better tumor targeting and longer blood retention time of PB@DN@M NPs derived from hybrid membrane. Compared with PB NPs, the amounts of PB@DN@M NPs accumulated in the liver and spleen was reduced due to the stealthy property of PB@DN@M NPs attributed to enrich proteins in macrophage cell membrane coating. Additionally, to ensure the PB@DN@M NPs contents in tumors, SERS imaging was achieved by the tumors collected from tumor-bearing mice after injected with PB@DN@M NPs for 24 h. A wide distribution of strong Raman signals at 2152 cm^{-1} was observed inside the tumor, especially in the dense locations of blood vessels (Additional file 1: Fig. S5). These results proved that PB@DN@M NPs had self-recognition ability and stealthy property at the cell as well as animal level.

Moreover, H&E staining of tumors from different groups were also investigated for assess the in vivo antitumor performance. Histologically, the tumor of the PB NPs with NIR irradiation and PB@DN@M NPs with NIR irradiation group exhibited a more remarkable structural destruction, while no obvious cell death was seen for the other groups (Additional file 1: Fig. S6). For the in vivo biosafety evaluation, H&E staining of the major organs from different groups in Additional file 1: Fig. S7 showed no significant cytoarchitectural alterations or inflammatory lesions in the major organs, which demonstrated the great biocompatibility of PB@DN@M NPs. Generally, the nuclear-targeted photothermal-chemotherapy induced by PB@DN@M NPs presented an extraordinary effect in inhibiting tumor growth in vivo.

Conclusions

In summary, we proposed a NIR-responsive biomimetic Prussian blue (PB) drug-loading nanotherapeutics (PB@DN@M) functionalized with tumor/nuclear targeting capability and immune escape ability, which exhibited an exciting tumor inhibition performance in vitro/vivo. The PB NPs possess a high photothermal conversion ability which hold a promising potential for photothermal applications. With hybrid membrane cloaking, the PB@DN@M NPs have both tumor targeting and immune escape ability, thus promoting the tumor aggregation. Furthermore, we exploit the NIR-responsive nuclear targeting/photothermal/chemotherapy all-in-one biomimetic PB nanotherapeutics (PB@DN@M) by the strategy of incorporation with the high-affinity peptides, which offers a boosted cellular internalization and nuclear entry efficiency. The in vitro/vivo experiment results have confirmed the remarkable antitumor performance of PB@DN@M NPs due to the increased enrichment inside tumor cells. Additionally, taking advantage of non-interference Raman nanotags of PB, it is promising to be served as a precision therapeutic tracker for guiding the photothermal-chemotherapy through SERS technique. In perspective, this NIR-responsive nuclear targeting/photothermal/chemotherapy biomimetic nanotherapeutics may contribute to specific treatment of various tumors.

Abbreviations

SERS	Surface-enhanced Raman spectroscopy
PB NPs	Prussian blue nanoparticles
DOX	Doxorubicin hydrochloride

NLS	Nuclear localization sequence peptides
HM	HepG2 cell membrane
RM	Raw 264.7 cell membrane
M	HepG2-Raw 264.7 hybrid cell membrane
PB@D	DOX-loaded PB
PB@DN	Nuclear targeting DOX-loaded PB
PB@DN@M	Hybrid cell membrane camouflaged PB@DN
CCK-8	Cell counting kit-8
ICP	Inductive coupled plasma emission spectrometer
TGI	Tumor growth inhibition
H&E	Hematoxylin and eosin

Supplementary Information

The online version contains supplementary material available at https://doi.org/10.1186/s12645-023-00224-4.

Additional file 1: Figure S1. Western blot analysis of different membrane protein for characterizing the presence of CD36 and CD81 in HepG2 membrane, Raw 264.7 membrane and the hybrid membrane vesicles. **Figure S2.** Fluorescent images of PB@D@M NPs incubated with VE cells, HeLa cells and HepG2 cells for 6 h. Scale bar: 50 μm. **Figure S3.** Fluorescent images of Raw 264.7 cells incubated with PB@D, PB@D@HM and PB@D@M NPs for 6 h. Scale bar: 50 μm. **Figure S4.** PB content was measured by ICP in HepG2 cells incubated with PB@HM, PB@RM, PB@M and PB@N@M NPs with/without NIR irradiation. ****P < 0.0001. **Table S1.** Tentative assignments of Raman fingerprints in the SERS spectra collected from the HepG2 cells. **Figure S5.** Photographic and SERS images based on the peak of 2152 cm^{-1} of tumor isolated from the mice injected with PB@DN@M NPs for 24 h. Scale bar: 100 μm. **Figure S6.** Representative images of H&E-stained tumors from the different treatment groups. Scale bar: 100 μm. **Figure S7.** H&E staining of major organs from different groups. Scale bar: 100 μm.

Author contributions

LZ and XX conceived and designed this project. XX performed the experiments, analyzed the data and wrote the manuscript. YZ took part in animal experiments. WZ, WC and CZ assisted the experiment. XL provided suggestions and technical support for this research. All authors read and approved the final manuscript.

Funding

This study was supported by the National Natural Science Foundation of China (62175041, 62275083 and 61727814).

Availability of data and materials

Data from this study are available within the article and its Supplementary Information files, or from the corresponding author upon reasonable request.

Declarations

Ethics approval and consent to participate

All animal experiments were carried out in accordance with the National Guidelines for Experimental Animal Welfare and Ethics (China) and approved by Institutional Animal Care and Use Committee of South China Normal University (No. SCNU-313388).

Consent for publication

All authors have seen the manuscript and approved the submission.

Competing interests

The authors declare no competing interests.

Received: 19 June 2023 Accepted: 15 August 2023
Published online: 03 October 2023

References

Ali MRK, Wu Y, Han T, Zang X, Xiao H, Tang Y et al (2016) Simultaneous time-dependent surface-enhanced Raman spectroscopy, metabolomics, and proteomics reveal cancer cell death mechanisms associated with gold nanorod photothermal therapy. J Am Chem Soc 138:15434–15442

Arabi L, Badiee A, Mosaffa F, Jaafari MR (2015) Targeting CD44 expressing cancer cells with anti-CD44 monoclonal antibody improves cellular uptake and antitumor efficacy of liposomal doxorubicin. J Controlled Release 220:275–286

Boateng F, Ngwa W (2020) Delivery of nanoparticle-based radiosensitizers for radiotherapy applications. Int J Mol Sci 21:273

Bose RJC, Kim BJ, Arai Y, Han I, Moon JJ, Paulmurugan R et al (2018) Bioengineered stem cell membrane functionalized nanocarriers for therapeutic targeting of severe hindlimb ischemia. Biomaterials 185:360–370

Bourquin J, Milosevic A, Hauser D, Lehner R, Blank F, Petri-Fink A et al (2018) Biodistribution, clearance, and long-term fate of clinically relevant nanomaterials. Adv Mater 30:1704307

Cai X, Gao W, Ma M, Wu M, Zhang L, Zheng Y et al (2015) A Prussian blue-based core–shell hollow-structured mesoporous nanoparticle as a smart theranostic agent with ultrahigh pH-responsive longitudinal relaxivity. Adv Mater 27:6382–6389

Cheng W, Tang P, He X, Xing X, Xing M, Lu L et al (2020) Dynamic monitoring and quantitative characterization of intracellular H2O2 content by using SERS based boric acid nanoprobe. Talanta 214:120863

Dhas N, García MC, Kudarha R, Pandey A, Nikam AN, Gopalan D et al (2022) Advancements in cell membrane camouflaged nanoparticles: a bioinspired platform for cancer therapy. J Controlled Release 346:71–97

Espinosa A, Silva AKA, Sánchez-Iglesias A, Grzelczak M, Péchoux C, Desboeufs K et al (2016) Cancer cell internalization of gold nanostars impacts their photothermal efficiency in vitro and in vivo: toward a plasmonic thermal fingerprint in tumoral environment. Adv Healthc Mater 5:1040–1048

Fu G, Liu W, Feng S, Yue X (2012) Prussian blue nanoparticles operate as a new generation of photothermal ablation agents for cancer therapy. Chem Commun 48:11567–11569

Harris JC, Scully MA, Day ES (2019) Cancer cell membrane-coated nanoparticles for cancer management. Cancers 11:1836

Her S, Jaffray DA, Allen C (2017) Gold nanoparticles for applications in cancer radiotherapy: mechanisms and recent advancements. Adv Drug Deliv Rev 109:84–101

Hu C-MJ, Zhang L, Aryal S, Cheung C, Fang RH, Zhang L (2011) Erythrocyte membrane-camouflaged polymeric nanoparticles as a biomimetic delivery platform. Proc Natl Acad Sci 108:10980–10985

Huang Z, McWilliams A, Lui H, McLean DI, Lam S, Zeng H (2003) Near-infrared Raman spectroscopy for optical diagnosis of lung cancer. Int J Cancer 107:1047–1052

Jędrzak A, Grześkowiak BF, Golba K, Coy E, Synoradzki K, Jurga S et al (2020) Magnetite nanoparticles and spheres for chemo- and photothermal therapy of hepatocellular carcinoma in vitro. Int J Nanomed 15:7923–7936

Jiang Q, Liu Y, Guo R, Yao X, Sung S, Pang Z et al (2019) Erythrocyte-cancer hybrid membrane-camouflaged melanin nanoparticles for enhancing photothermal therapy efficacy in tumors. Biomaterials 192:292–308

Kalderon D, Roberts BL, Richardson WD, Smith AE (1984) A short amino acid sequence able to specify nuclear location. Cell 39:499–509

Kapara A, Brunton V, Graham D, Faulds K (2020) Investigation of cellular uptake mechanism of functionalised gold nanoparticles into breast cancer using SERS. Chem Sci 11:5819–5829

Knop K, Hoogenboom R, Fischer D, Schubert US (2010) Poly(ethylene glycol) in drug delivery: pros and cons as Well as potential Alternatives. Angew Chem Int Ed 49:6288–6308

Li Y, He D, Tu J, Wang R, Zu C, Chen Y et al (2018a) The comparative effect of wrapping solid gold nanoparticles and hollow gold nanoparticles with doxorubicin-loaded thermosensitive liposomes for cancer thermo-chemotherapy. Nanoscale 10:8628–8641

Li J, Zhen X, Lyu Y, Jiang Y, Huang J, Pu K (2018b) Cell membrane coated semiconducting polymer nanoparticles for enhanced multimodal cancer phototheranostics. ACS Nano 12:8520–8530

Li M, Xu Z, Zhang L, Cui M, Zhu M, Guo Y et al (2021) Targeted noninvasive treatment of choroidal neovascularization by hybrid cell-membrane-cloaked biomimetic nanoparticles. ACS Nano 15:9808–9819

Lin X, Cao Y, Li J, Zheng D, Lan S, Xue Y et al (2019) Folic acid-modified prussian blue/polydopamine nanoparticles as an MRI agent for use in targeted chemo/photothermal therapy. Biomater Sci 7:2996–3006

Liu Y, Luo J, Chen X, Liu W, Chen T (2019) Cell membrane Coating Technology: a promising strategy for Biomedical Applications. Nano-Micro Lett 11:100

Liu R, An Y, Jia W, Wang Y, Wu Y, Zhen Y et al (2020) Macrophage-mimic shape changeable nanomedicine retained in tumor for multimodal therapy of breast cancer. J Controlled Release 321:589–601

Liu Y, Sukumar UK, Kanada M, Krishnan A, Massoud TF, Paulmurugan R (2021a) Camouflaged hybrid cancer cell-platelet fusion membrane nanovesicles deliver therapeutic MicroRNAs to presensitize triple-negative breast cancer to doxorubicin. Adv Funct Mater 31:2103600

Liu R, Sang L, Wang T, Liu Y, Wang Z, Li J et al (2021b) Phase-change mesoporous prussian blue nanoparticles for loading paclitaxel and chemo-photothermal therapy of cancer. Colloids Surf B Biointerfaces 207:112018

Liu H, Mo L, Chen H, Chen C, Wu J, Tang Z et al (2022) Carbon dots with intrinsic bioactivities for photothermal optical coherence tomography, tumor-specific therapy and postoperative wound management. Adv Healthc Mater 11:2101448

Maiti KK, Dinish US, Samanta A, Vendrell M, Soh K-S, Park S-J et al (2012) Multiplex targeted in vivo cancer detection using sensitive near-infrared SERS nanotags. Nano Today 7:85–93

Maity AR, Stepensky D (2016) Efficient subcellular targeting to the cell nucleus of Quantum Dots densely decorated with a Nuclear localization sequence peptide. ACS Appl Mater Interfaces 8:2001–2009

Nair JB, Joseph MM, Arya JS, Sreedevi P, Sujai PT, Maiti KK (2020) Elucidating a thermoresponsive multimodal photochemotherapeutic nanodelivery vehicle to overcome the barriers of doxorubicin therapy. ACS Appl Mater Interfaces 12:43365–43379

Nel AE, Mädler L, Velegol D, Xia T, Hoek EMV, Somasundaran P et al (2009) Understanding biophysicochemical interactions at the nano–bio interface. Nat Mater 8:543–557

O'Brien MER, Wigler N, Inbar M, Rosso R, Grischke E, Santoro A et al (2004) Reduced cardiotoxicity and comparable efficacy in a phase III trial of pegylated liposomal doxorubicin HCl(CAELYX™/Doxil®) versus conventional doxorubicin forfirst-line treatment of metastatic breast cancer. Ann Oncol 15:440–449

Pallares RM, Abergel RJ (2020) Nanoparticles for targeted cancer radiotherapy. Nano Res 13:2887–2897

Pan L, He Q, Liu J, Chen Y, Ma M, Zhang L et al (2012) Nuclear-targeted drug delivery of TAT peptide-conjugated monodisperse mesoporous silica nanoparticles. J Am Chem Soc 134:5722–5725

Panikkanvalappil SR, James M, Hira SM, Mobley J, Jilling T, Ambalavanan N et al (2016a) Hyperoxia induces intracellular acidification in neonatal mouse lung fibroblasts: Real-Time Investigation using plasmonically enhanced Raman Spectroscopy. J Am Chem Soc 138:3779–3788

Panikkanvalappil SR, Hira SM, El-Sayed MA (2016b) Elucidation of ultraviolet radiation-induced cell responses and intracellular biomolecular dynamics in mammalian cells using surface-enhanced Raman spectroscopy. Chem Sci 7:1133–1141
Qi G, Zhang Y, Xu S, Li C, Wang D, Li H et al (2018) Nucleus and Mitochondria Targeting Theranostic Plasmonic Surface-Enhanced Raman Spectroscopy Nanoprobes as a Means for revealing molecular stress response differences in Hyperthermia Cell death between cancerous and normal cells. Anal Chem 90:13356–13364
Rodriguez PL, Harada T, Christian DA, Pantano DA, Tsai RK, Discher DE (2013) Minimal "Self" peptides that inhibit phagocytic clearance and enhance delivery of nanoparticles. Science 339:971–975
Shen Y, Liang L, Zhang S, Huang D, Deng R, Zhang J et al (2018) Organelle-targeting gold nanorods for macromolecular profiling of subcellular organelles and enhanced Cancer Cell Killing. ACS Appl Mater Interfaces 10:7910–7918
Shokouhimehr M, Soehnlen ES, Hao J, Griswold M, Flask C, Fan X et al (2010) Dual purpose prussian blue nanoparticles for cellular imaging and drug delivery: a new generation of T1-weighted MRI contrast and small molecule delivery agents. J Mater Chem 20:5251–5259
Singh R, Norret M, House MJ, Galabura Y, Bradshaw M, Ho D et al (2016) Dose-dependent therapeutic distinction between active and Passive Targeting revealed using transferrin-coated PGMA nanoparticles. Small 12:351–359
Singh N, Gupta A, Prasad P, Sah RK, Singh A, Kumar S et al (2021) Mitochondria-targeted photoactivatable real-time monitoring of a controlled drug delivery platform. J Med Chem 64:17813–17823
Tammam SN, Azzazy HME, Lamprecht A (2016) How successful is nuclear targeting by nanocarriers? J Controlled Release 229:140–153
Tang P, Xing M, Xing X, Tao Q, Cheng W, Liu S et al (2021) Receptor-mediated photothermal/photodynamic synergistic anticancer nanodrugs with SERS tracing function. Colloids Surf B Biointerfaces 199:111550
Terentyuk G, Panfilova E, Khanadeev V, Chumakov D, Genina E, Bashkatov A et al (2014) Gold nanorods with a hematoporphyrin-loaded silica shell for dual-modality photodynamic and photothermal treatment of tumors in vivo. Nano Res 7:325–337
Wang D, Dong H, Li M, Cao Y, Yang F, Zhang K et al (2018) Erythrocyte–cancer hybrid membrane camouflaged hollow copper sulfide nanoparticles for prolonged circulation life and homotypic-targeting photothermal/chemotherapy of melanoma. ACS Nano 12:5241–5252
Wang S, Wang R, Meng N, Guo H, Wu S, Wang X et al (2020) Platelet membrane-functionalized nanoparticles with improved targeting ability and lower hemorrhagic risk for thrombolysis therapy. J Controlled Release 328:78–86
Xie Y, Tang P, Xing X, Zhao Y, Cao S, Liu S et al (2020) In situ exploring Chidamide, a histone deacetylase inhibitor, induces molecular changes of leukemic T-lymphocyte apoptosis using Raman spectroscopy. Spectrochim Acta A Mol Biomol Spectrosc 241:118669
Yang Y, Nie D, Liu Y, Yu M, Gan Y (2019) Advances in particle shape engineering for improved drug delivery. Drug Discov Today 24:575–583
Yin Y, Li Q, Ma S, Liu H, Dong B, Yang J et al (2017) Prussian Blue as a highly sensitive and background-free resonant Raman reporter. Anal Chem 89:1551–1557
Zhao Y, Tang P, He X, Xie Y, Cheng W, Xing X et al (2020) Study on the precise mechanism of Mitoxantrone-induced Jurkat cell apoptosis using surface enhanced Raman scattering. Spectrochim Acta A Mol Biomol Spectrosc 228:117718
Zhu W, Gao M-Y, Zhu Q, Chi B, Zeng L-W, Hu J-M et al (2020) Monodispersed plasmonic prussian blue nanoparticles for zero-background SERS/MRI-guided phototherapy. Nanoscale 12:3292–3301

Publisher's Note